Testing Power Law Models of Drop Pinch-Off Radii

Perrin W. Davidson*
UChicago Department of Physics
(Dated: November 2, 2021)

We estimate the minimum drop pinch-off radius, R_{min}, of an aqueous glycerine drop using simple power law models in two regimes. Utilizing high speed photography, we estimate R_{min} using a computer vision algorithm. We then fit these data using a generalized, non-linear least-squares method. We compare the fitted power parameters to two models derived from dimensional analysis and simple power law relationships. Our results are not consistent with the canonical power law models and instead predict an R_{min} power dependence of $\alpha = 0.76$ in the surface tension-driven Regime 1 and $\alpha = 0.94$ in the viscosity-driven Regime 2 on time from pinch-off. We attribute both the simplistic nature of the power law models that do not take into consideration more complex processes of our drop pinch-off, the precision of our high speed footage, and other systematic biases to this discrepancy.

I. INTRODUCTION

In fluid dynamics, power law models are fundamental to a first-order understanding of incredibly complex processes [1]. In this experiment, we use high-speed photography to determine the time evolution of the minimum drop pinch-off radius, R_{min}, and test our observational data against two power law regimes.

Fundamentally, there are a few values that will be to leading order driving the process of the drop pinch-off. These are: surface tension (γ, [M] [T]$^{-2}$), fluid density (ρ, [M] [L]$^{-3}$), and viscosity (g, [M] [L]$^{-1}$ [T]$^{-1}$). Here, we are generalizing the units using brackets, where [M] is a unit of mass, [L] is a unit of length, and [T] is a unit of time.

I.1. Pinch-Off Regimes

The first regime is just as the drop is beginning to separate from the nozzle. At this time, the major forces at play are those which are trying to minimize the shape of the deforming viscous aqueous glycerine solution. Therefore, this first regime is surface tension-driven. Additionally, we consider the relative magnitudes of other forces at play — such as gravitational potential — at the scales we are interested in, namely those on the length and time scales of droplet formation. In this limit, we find that to leading order the interplay between surface tension and density will be the most important contributions. Taking into account the relative contributions of each of these quantities, and performing dimensional analysis using the units presented above, we find that the power law relationship between R_{min} in units of [L] and time, τ, in units of [T] is:

$$R^1_{min} = \left(\frac{[L]^2}{[T]^2}\right)^{1/3}[T]^{2/3} \tag{1}$$

$$= \left(\frac{\gamma}{\rho}\right)^{1/3}\tau^{2/3}, \tag{2}$$

where:

$$\tau = t_0 - t, \tag{3}$$

with t_0 the pinch-off time determined as the first time at which the drop fully separates from the nozzle and t is the absolute time measurement of the frame.

Similarly, as the droplet starts to move toward completely separating, the roles switch, and the importance of viscosity — or the resistance of the drop to deformation — can be seen in studying the drop. Again studying the relative magnitudes and scales of interest, we find that the second regime is in the viscosity-driven limit. Here, we find that quantities that are driving the pinch-off process are viscosity and surface tension. Again performing dimensional analysis, we find that the equation for R_{min}'s dependence on τ is:

$$R^2_{min} = \left(\frac{[L]}{[T]}\right)[T] \tag{4}$$

$$= \left(\frac{\gamma}{\eta}\right)\tau. \tag{5}$$

Looking at Eq. (2) and Eq. (5), we can see that each of these power law models is off the form:

$$R^i_{min} = C_0\tau^\alpha, \tag{6}$$

where C_0 is a constant dependent on the physical parameters of the fluid, specifically density, surface tension, and viscosity. α is the power parameter relating these physical parameters and time, τ. Essentially, the bulk of this work is to find the exponent (i.e., "power") of time τ of the form [L] $\sim$ [T]$^\alpha$, where α is the exponent power of interest. We will use Eq. (6) to fit our radii measurements from high speed photography to estimate these cœfficients and, thereby, the experimentally determined powers of each regime. We will then compare these to the canonical, theoretical values obtained from Eq. (2) and Eq. (5).
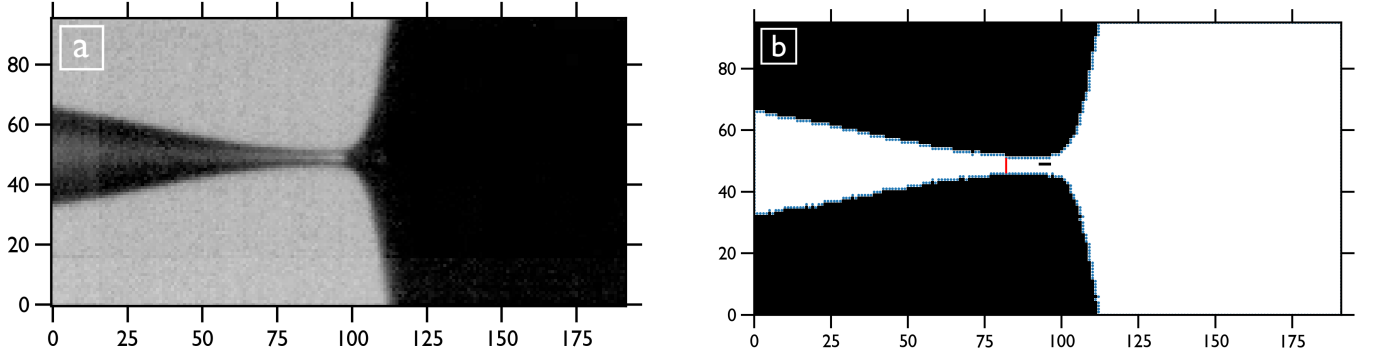
* pwd@uchicago.edu

FIG. 1: (a) Frame 57 from our high-speed photography experiment with a resolution of 96 pixels by 192 pixels, an FPS of 38,565, a minimum period of 25.93 μs, exposure of 20.98 s, and gain of 0 dB. (b) The computer-vision thresholded and contoured Frame 57 from (a). The blue pixels are the contour of the drop, and the vertical red line is the minimum radius as determined by our algorithm.

II. METHODS AND MATERIALS

II.1. High Speed Photography

To capture our drop pinch-off radii, we utilized high speed photography. Specifically, we used a high speed camera to capture a series of videos at a resolution of 92 pixels by 192 pixels, the minimum resolution of the camera. This allowed us to shoot at the highest possible frame per second (FPS) of the camera, at 38,565 FPS. An example of a frame from this captured video is presented in Fig. 1. The minimum period of the camera was at 25.93 μs, the exposure was at 20.98 seconds, and the gain was set to 0 dB. A total of 15 videos were taken over a range of resolutions, before the 14th such video was chosen (filenamed `dpo_14.mp4`) with the characteristics described above.

II.2. R_{min} Determination

To determine the R_{min} used to estimate our power law α, we conducted two methods. The first was a subjective, visually inspected method. For this method, we used `ImageJ` to select 20 datapoints across the video of interest to estimate the minimum pinch-off radius. We recoreded these values both in a laboratory notebook and an excel spreadsheet (filenamed `radii_min.xlsx`). The resolution of this process was 0.12 pixels. To use `ImageJ`, we used `FFMpeg` to convert our `dpo_14.mp4` to `dpo_14.avi`. However, after an initial analysis with the data, we found that this method was to subjective to be used in our analysis.

Therefore, we used an objective, computer vision-based (CV) method. To begin this method, we first adjusted the contrast and brightness of our video using `cv2` to optimize the efficacy of the objective method. Then, we used the same `cv2` Python package to first threshold and invert our adjusted image. Next, any pixel that was darker than 58 on the RGB scale was turned to white and lighter than 58

was turned black (note the inversion). 58 was determined subjectively to ensure the best contouring results. This then allowed us to use the `cv2` to contour the image, finding the greatest complete contour of the image per frame, as see in 1. Next, the minimum distance between this contour at the same horizontal pixel position was calculated and determined as R_{min} for that frame. This process proceeded from the first frame until the calculated radius was 0, which occurred at frame 63.

Given that the resolution of this method is exactly 1 pixel, there were numerous consecutive, duplicated radii in a row that were completely driven by the precision of the camera. To combat this, the 63 computed radii were binned by radii (only if they were consecutive) and their time averaged. Therefore, the fit would be more physically consistent rather than having to fit multiply duplicated values. As the average time value was taken (i.e., optimally placed for the fitting performed later), and the radii were unaffected by this averaging, we assumed that this process introduced no error. 27 data points were removed this way.

Lastly, after an initial log-log plotting of the data, 8 data points were removed from our dataset as they were determined by CV but were not physically consistent with the minimum radius given the crop of the image. This process of averaging and reliably quality controlling the data lead to a final dataset of 26 radii. The same initial plotting described above led us to bin the data into two regimes, as described in Sec. I.1. This gave a binning of 17 data points in Regime 1 and 9 data points in Regime 2.

II.3. Image Calibration

Note that the co-ordinates from Sec. II.2 are (frames, pixels). These units need to be calibrated to more physically significant units. To do this, we took a high speed video of a metric ruler at the same settings as those presented in Sec. II.1. We measured the distance between two millimeter markings in `ImageJ`, centering the cursor over each mark-
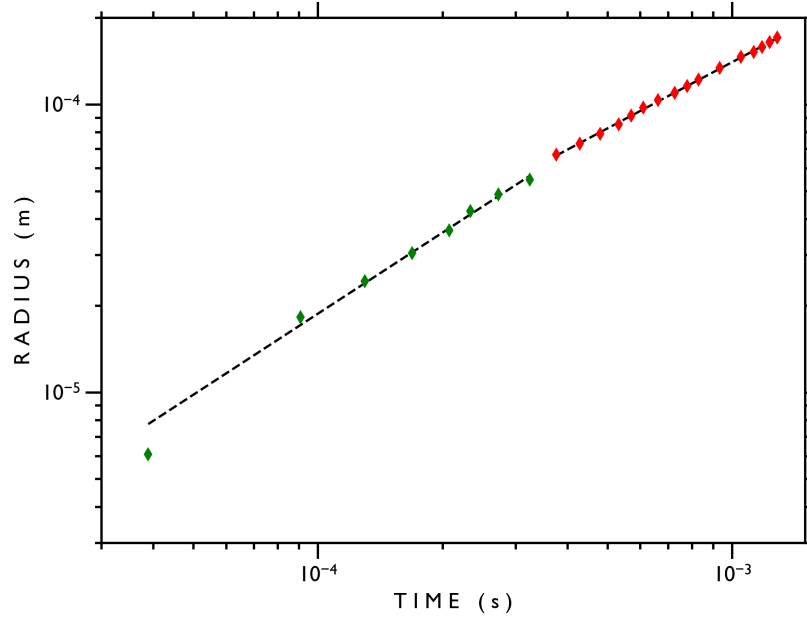
Parameter	Regime 1	Regime 2
C_0	0.02755 (m s $^{-1}$)	0.1043 (m s $^{-1}$)
α	0.7642	0.9361

Regime	χ^2	χ^2_ν	N_ν
Regime 1	$\mathcal{O}(8)$	$\mathcal{O}(7)$	14
Regime 2	$\mathcal{O}(9)$	$\mathcal{O}(8)$	7

FIG. 2: The plot shows the fitted radii in the binned regimes. The first regime is plotted in red diamonds, and the second regime is plotted in green diamonds. The fits of each regime to these points using the Levenberg-Marquadt (LM) algorithm implementation of the generalized non-linear least squares method are the dashed black lines. Note that the errors for each of these radii calculated using Eq. (10) are smaller than the diamond markers themselves and are thus not seen in the plot. Additionally, the data point of 0 m radius is not plotted as the log-log plot used in this figure dœs not effectively visualize this point. The upper table shows the fitted values from the LM method, both the amplitude-like physical constant, C_0, and the power exponent, α. Please note that uncertainties in these predictions are on the order of $\mathcal{O}(-6)$ or less and are therefore not presented in the table, as given the significant figures of the parameter estimates would be given as 0.0000. The lower table shows the goodness of fit (GoF) for each fitting by the LM method. The exact numbers are not exactly stated as they are so large their exact quantities are nearly meaningless.[a]

[a] The exact values for each regime are, of the form (χ^2, χ^2_ν): $(7.361 \times 10^8, 5.258 \times 10^7)$ for Regime 1 and $(3.938 \times 10^9, 5.626 \times 10^8)$ for Regime 2.

ing. This distance was then multiplied by 1000 to get the number of pixels per meter, namely c_{px}. The error in this estimate was taken as the width of each of thes markings, Δc_{px}. Then, the following conversion was used:

$$R_{min}(\text{m}) = \frac{R_{min}(\text{px})}{c_{px}}. \tag{7}$$

To calibrate the time, we know the FPS value from Sec. II.1. Defining this as c_{fps}, we used the following conversion rela-

tion to turn units of frames to units of seconds:

$$t(\text{s}) = \frac{t(\text{frame})}{c_{fps}}. \tag{8}$$

Explicitly, we take: $c_{fps} = 3.8565 \times 10^4$ (frames s^{-1}) and $c_{px} = 1.6409 \times 10^6 \pm 2.9360 \times 10^4$ (pixel m^{-1}).
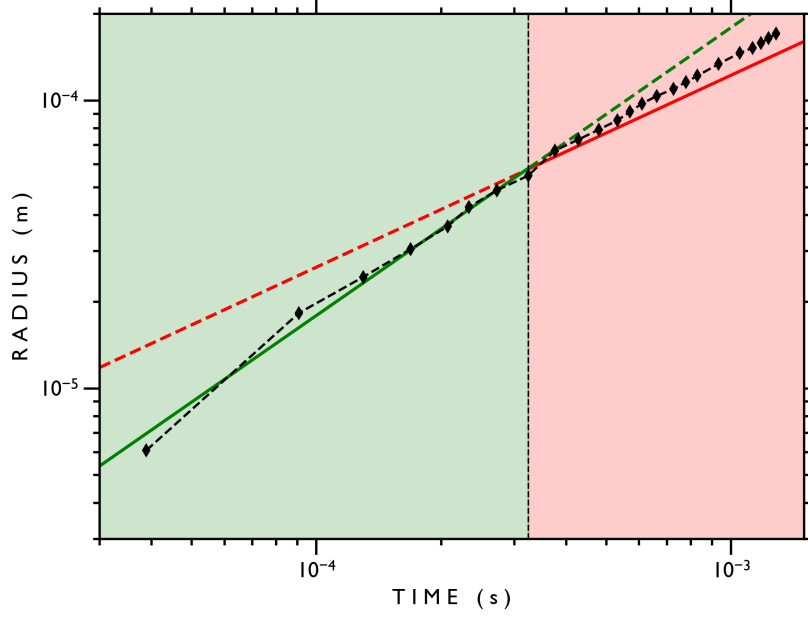
FIG. 3: Idealized power laws plotted against observational data. The regimes are marked by colors as done in Fig. 2. The red solid line presents the Regime 1 power law of $\alpha = 2/3$, which extends the entirety of the red polygon, or until the vertical black dotted line. The solid green line is the Regime 2 power law of $\alpha = 1$ which extends for the entirety of the green polygon. Note that each regime power law function is dotted in the region that it does not correspond to. These idealized functions are of the form presented in Eq. (6), with the C_0 tuned to match the observational data best.

II.4. Uncertainties

Given the conversion relations presented in Eq. (7) and Eq. (8), we need to determine the error in our radii measurements. First, we will apply the following error propagation formula [2]:

$$\Delta f = \sqrt{\sum_i \left(\frac{\partial f}{\partial x_i} \Delta x_i \right)^2} \qquad (9)$$

Then, we know that the precision of the CV method was 1 pixel. Define this as ΔR_{min}. Along with Δc_{px} and applying Eq. (9) to Eq. (7), we get the following error propagation formula for our radii measurements:

$$\Delta R_{min}(\mathsf{m}) = \sqrt{\left(\frac{\Delta R_{min}(\mathsf{px})}{c_{px}} \right)^2 + \left(\frac{R_{min}(\mathsf{px})}{c_{px}^2} \Delta c_{px} \right)^2}. \qquad (10)$$

Given that $c_{fps} = 3.8565 \times 10^4$ (frames s^{-1}), we take the error from the measurement of time to be negligible as one frame is on the order of 10^{-3} to 10^{-4} seconds. This is a consequence of the trade off between temporal and spatial resolution of the camera, of which we chose the temporal resolution in order to capture the drop pinch-off process with high fidelity.

II.5. Least-Squares Fitting

To estimate the powers of α in this experiment, we use a generalized, non-linear least squares method. The function fit to the estimated radii from Sec. II.2 is Eq. (6), as it is a generalized form of the theoretical, power law-derived equations for both regimes. The uncertainties for the least-squares parameters C_0 and α as presented in Eq. (6) were calculated from the Levenberg-Marquadt algorithm implementation of this least squares method. The method works to minimize the squared sum of the fit residuals normalized by the uncertainty, ϵ:

$$\chi^2 = \sum_{i=1}^{N-1} \left(\frac{\widehat{y}_i - y_i}{\epsilon_i} \right)^2, \qquad (11)$$

where $\widehat{y}_i$ is the fit value and y_i the measured value. The uncertainty in each estimated parameter is determined by the variance in the parameter estimate, given generically for a parameter function $\Theta(\boldsymbol{x})$ by [3]:

$$\sigma_\Theta^2 = \sum_{t=0}^{N-1} \sigma_i^2 \left(\frac{\partial \Theta}{\partial x_i} \right)^2 \qquad (12)$$

where $x_i \in \boldsymbol{x}$ are the parameters being fit and σ_i^2 the variance in each parameter fit. The χ^2 goodness of fit statistic

was calculated following :

$$\chi^2 = \sum_{i=1}^{N} \left(\frac{\widehat{y}_i - y_i}{\epsilon_i} \right)^2, \tag{13}$$

similar in construction to Eq. (11). The Degrees of Freedom were calculated following:

$$N_\nu = \text{length}(y) - \text{length}(x) \tag{14}$$

where y are the number of data points being fitted and x are the parameters being fitted.

III. RESULTS

The results from least-squares fitting routine discussed in Sec. II.5 are presented in the plot of Fig. 2, along with the estimated radii, R_{min} discussed in Sec. II.2. The estimated parameters from the fitting routine are presented in the top table of Fig. 2. Please note that the uncertainties in the radii calculated using Eq. (10) are less than the markers so cannot be visibly seen. Additionally, the error in the parameter estimates are less than -2 orders of magnitude less than the significant figures of the parameters so are chosen not to be presented in the table.[1]

The two regimes are clearly divided, and the two slopes of each regime can clearly be seen in Fig. 2. Note the increase in slope between the first and second regimes, as the change between surface tension and viscosity takes over. The log-log plot was chosen to better visualize the power relationships of the fitted functions.

The time extent of Regime 1 is from $\tau = 3.24 \times 10^{-4}$ seconds to $\tau = 1.28 \times 10^{-3}$ seconds. The time extent of Regime 2 is from $\tau = 0$ seconds to $\tau = 3.24 \times 10^{-4}$ seconds. Note that $\tau = 3.24 \times 10^{-4}$ seconds is the transition point in the observational data between Regime 1 and Regime 2. At this point, the powers of the fitted power law relationships change, from 0.764 to 0.936. The ranges of radii, R_{min}, for each regime are from $R_{min}^1 = 5.48 \times 10^{-5}$ meters to $R_{min}^1 = 1.71 \times 10^{-4}$ meters and $R_{min}^2 = 0$ meters to $R_{min}^2 = 5.48 \times 10^{-5}$ meters, respectively. Therefore, there is a critical point at $(3.24 \times 10^{-4}, 5.48 \times 10^{-5})$ at which point the regimes change.

Additionally, note that at this point the cœfficients of the power law relationships, C_0, also change. This value increases from 0.0276 (m s $^{-1}$) to 0.104 (m s $^{-1}$). These values are also related to the ratios of surface tension and density and surface tension and viscosity, respectively for Regimes 1 and 2. Specifically, we can determine the ratios as follows. For Regime 1, we know that C_0 is 1/3rd the ratio of surface tension to density. Therefore, we can calculate this ratio as $\gamma : \rho = 0.0276^3 = 2.09 \times 10^{-5}$ [L]^3 [T]$^{-3}$.

---

[1] Respectively these uncertainties are, of the form (C_0, α): $(1.505 \times 10^{-7}, 7.598 \times 10^{-7})$ for Regime 1 and $(1.271 \times 10^{-6}, 1.440 \times 10^{-6})$ for Regime 2.

We can then calculate the ratio of the second regime as $\gamma : \eta = 0.104$ [L] [T]$^{-1}$. We lastly calculate the ratio of $\eta : \rho = C_0^1/C_0^2 = 2.01 \times 10^{-4}$ [L]^2 [T]$^{-1}$. Again, for these values the errors are less than $\mathcal{O}(-2)$ less than the the estimates' significant figures so are negligible in the presentation here. These basic manipulations now give us some physical intuition and constraints on the relationship between the parameters of our system and viscous aqueous glycerine drop.

IV. DISCUSSION

IV.1. Parameter Estimation

From Eq. (2), we know that the power law relationship for the surface tension-driven Regime 1 gives a power of $\alpha = 2/3$. From the fitted data of Regime 1, we obtain a power of $\alpha = 0.7642 \pm 0.0000$. Our estimated parameter of this relationship is, therefore, not within error bounds for the theoretical value. We can calculate the percent error following [4]:

$$\%\Delta = \frac{|x - \widehat{x}|}{x} \times 100\%, \tag{15}$$

where x is the theoretical value and $\widehat{x}$ is the experimental value. We get that our Regime 1 power law has a percent error of 14.63%. While Eq. (5) gives an $\alpha = 1$ for Regime 2, we get an experimentally fitted $\alpha = 0.9361 \pm 0.0000$, which is also not within the error bounds of the literature value. The percent error for Regime 2 is 6.394%. Therefore, our data for Regime 2 is closer to the theoretical value than in Regime 1.

However, despite this error, note Fig. 3, which presents idealized versions of the power law relationships, i.e., with exponents from the theory. Regime 1 is in the red region, and Regime 2 is in the green region. The correspondingly colored lines are the predicted theoretical power law relationships, solid in the regions in which they are valid and dashed outside of these regions. The C_0 values here are tuned for optimal plotting and comparison. While we are not within certainty of these theoretical values, it is clear upon visual inspection that the general trend of our data closely resembles that of the theoretically predicted values.

Interestingly, the data in Regime 1 follows a slightly different power law, while the data in Regime 2 is more closely spread about the theoretical value, as is indicated by the difference of more than 2 times between each regime's $\%\Delta$ (i.e., there is less percent error in the Regime 2 power estimation than in Regime 1). This implies that our discrepancy of the power law of Regime 1 is based less on statistical and/or systematic biases and more so on the fundamental scaling laws used to derive the power law.

We attribute the differences between the theoretical powers and our experimental powers to the simplistic derivation behind these power law relationships. With just dimensional analysis, we were able to derive a nearly realistic depiction of the real world. However, we believe that it might be overly simplistic and dœs not take into consideration all possible,
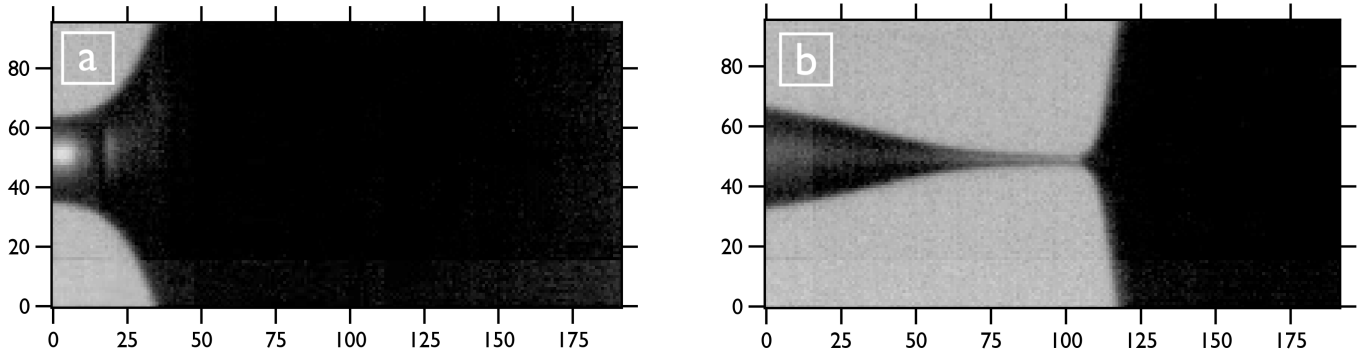
FIG. 4: Regime differences in drop radii. (a) Regime 1 of the drop pinch-off as seen by the high speed camera, taken at Frame 12. Note the hyperbolic contour that increase in width as the horizontal pixels increases toward the drop pinch-off point. (b) Regime 2 of the drop pinch-off as seen by the high speed camera, taken at Frame 60. Note that rapid decay of the contour toward the final pinch-off as the horizontal pixels approach the drop pinch-off point.

complex processes of the water drop. For instance, taking into consideration the effects of inter-molecular forces, interactions at the nozzle interface, and the effect of the external environment on the drop would change the final formulation of the equation describing the drop pinch of radius.

IV.2. Physical Insights of Regimes

Fig. 4 displays the two difference regimes as seen by the high speed camera. Specifically, (a) is at Frame 12 in Regime 1 and (b) is at Frame 60 in Regime 2, on either end of the time period of τ in the video used in this analysis. The difference in shape can clearly be seen here. Starting at the 0 pixel mark, if one proceeds to the right — toward what we will call the "droplet", or the point of pinch-off — the curvature of the contours of the drop are different. Specifically, in Regime 1, the curvature is nearly hyperbolic, while in Regime 2, the drop contour steadily decays as it approaches the droplet.

This is physical evidence of the two difference regimes that we are exploring in this experiment. Specifically, remember that Regime 1 is the surface tension-driven regime. This is reflected in the shape, namely the greater radii and the tendency toward minimizing the surface area while changing shape. Then, in Regime 2 — the viscosity-driven limit — we can see that it is clearly the last bit of this viscous fluid resisting the deformation of the droplet detaching. Immediately before the pinch, it is the viscosity that is leading the charge toward resisting any change. This is clearly not a minimization of surface area, which is surface tension's role in Regime 1. Therefore, we can see visual, physical evidence for the two power law regimes described in Sec. I.1.

IV.3. Possible Uncertainties

There are numerous uncertainties and sources of error that need to be addressed in this work. The first of these is a systematic bias: the resolution of the high speed camera. This is perhaps the greatest source of precision-related error in the experiment. Given the low spatial resolution of the high speed camera — which we sacrificed for temporal resolution — the CV method by which we determined the minimum radius, R_{min} was limited to the 1 pixel resolution. This lead us to temporally average consecutively similar radii. This entire process introduces error into our experiment that could have been avoided if the spatial resolution of the camera was better, leading to there not being a large number of duplicate values in a row. A possible solution to this, besides upgrading the camera and thereby the resolution, is to interpolate the image to a greater pixel dimension. However, this would introduce its own sets of biases and error. Correspondingly, the use of minimum variance techniques, i.e., kriging, could be explored.

The second source of uncertainty in our experiment is the use of `ImageJ` in determining the pixel to meter conversion. While we were careful in our selection of the midpoint of each marking on the ruler, this method is still somewhat crude. One way to fix this in future experiments is to use a similar CV method that is adapted to colored markings on the ruler from the contour of the drop. Initial experiments proved this to be a hard process and is something to improve upon in the future.

Another major area of uncertainty are the GoF values for the fits performed, presented in the lower table of Fig. 2. When fitting these data at the pixel-based level — before applying the pixel to meter conversion stated in Eq. (7) — these GoF values were on the order of $\mathcal{O}(1)$. Therefore, we believe that the high magnitude of these values is directly proportionally the small magnitudes of each measurement, as well as the small error for each measurement given by Eq. (10) in relation to these measurement magnitudes. As the LM method takes into consideration these weights, the smaller these errors, the harder it is for the fitting procedure to accurately fit the function within the given errors, leading to the large GoF values. These GoF values do not give us quantitative confidence in the fitting of our data with the

power law models. However, the visual inspection of the data, such as in Fig. 2, does inspire some confidence in our fitting method and technique.

V. CONCLUSION

We conclude that while powerful and, to some extent, accurate, the power law relationships derived from dimensional analysis are not consistent with our experimental data. We find that in the surface tension-driven Regime 1 of a drop pinch-off process, the power relationship is approximately $\alpha = 0.76$ and in the viscosity-driven Regime 2, the power relationship is approximately $\alpha = 0.94$. This is contrasted against the theoretically derived $\alpha = 2/3$ and $\alpha = 1$ for Regimes 1 and 2, respectively. We attribute this discrepancy to the simplistic derivation of the power law relationships. Despite this, our experiment does reinforce the validity of dimensional analysis as a tool to, to first order within some given percentage error, approximate physical processes of the real world with minimal effort.

[1] M. Chantell, D. McCowan, and K. V. D. Bogart, *Drop Pinch Off*, Department of Physics, The University of Chicago (2021).

[2] M. Chantell, D. McCowan, and K. V. D. Bogart, *Uncertainty Analysis and Significant Digits*, Department of Physics, The University of Chicago (2021).

[3] M. Chantell, D. McCowan, and K. V. D. Bogart, *Linear Least-Squares Fitting*, Department of Physics, The University of Chicago (2021).

[4] D. of Physics and Astronomy, *Percent Error Formula*, University of Iowa (2017).